AGU PUBLICATIONS

Geophysical Research Letters

Supporting Information for

Harnessing Satellite Data Alone for Mapping Global Thermal Anisotropy

Wenfeng Zhan[1, 2, 3], Huilin Du[1*], Zihan Liu[1], Jiufeng Li[1], TC Chakraborty[4], Fan Huang[1]

[1]Jiangsu Provincial Key Laboratory of Geographic Information Science and Technology, International Institute for Earth System Science, Nanjing University, Nanjing, China

[2]Jiangsu Center for Collaborative Innovation in Geographical Information Resource Development and Application, Nanjing, China

[3]Frontiers Science Center for Critical Earth Material Cycling, Nanjing University, China

[4]Atmospheric Sciences and Global Change Division, Pacific Northwest National Laboratory, Richland, USA

Contents of this file

Introduction

Supporting information includes eight texts (Texts S1 to S8) and thirteen figures (Figures S1 to S29).

- Text S1 shows the research progress and challenges of previous studies;
- Text S2 shows the elaborate steps on thermal anisotropy mapping across global lands;
- Text S3 shows the potential uncertainties related to the impacts from land cover changes over the study period;
- Text S4 shows the potential impacts from retrieval errors in various MODIS products;
- Text S5 shows the potential impacts from directionalities in atmospheric attenuation and emissivity inherent in MODIS LST products;
- Text S6 shows the potential uncertainties related to the interval number for

spatially and temporally categorizing MODIS LST pixels;

- Text S7 shows the reasons for the greater TAI variations with SAT than RAD and the relatively low RAD values;
- Text S8 shows the clarifications on the robustness of TAI patterns over arid regions.

- Figure S1 denotes the comprehensive framework for surface thermal anisotropy intensity (TAI) mapping across global lands;
- Figure S2 shows the spatial distribution of downward shortwave radiation (RAD; W/m^2) averaged over all summer afternoons from 2003 to 2022;
- Figure S3 shows the spatial distribution of the grids used for examining the relationships between TAI and two atmospheric parameters during summer afternoon;
- Figure S4 shows the global mapping of thermal anisotropy intensity (TAI) from 2003 to 2022;
- Figure S5 gives the TAI curves for different sensor VZAs during summer daytime across all climate zones;
- Figure S6 gives the spatial patterns of TAI during summer mornings over several typical desert surfaces worldwide, alongside their corresponding topographic maps;
- Figure S7 shows the contributions of various factors to surface TAI across three typical regions of the Sahara Desert;
- Figure S8 shows the 1:1 scatterplot comparing the observed and estimated TAI values across three typical regions of the Sahara Desert;
- Figure S9 gives the photos of undulating sand dunes over typical deserts;
- Figure S10 shows the spatial patterns of TAI during summer mornings and afternoons across typical African regions, alongside the corresponding land cover types;
- Figure S11 gives the spatial patterns of TAI across three typical regions, along with their corresponding thermal anisotropy curves;
- Figure S12 shows the number of Aqua LST images across different sensor VZA intervals during summertime from 2003 to 2022 over typical African regions;
- Figure S13 shows the variations in TAI depending on surface parameters during summer daytime;
- Figure S14 shows the variations in TAI depending on elevation standard deviation (σ_{ele}) during summer daytime;
- Figure S15 shows the variations in TAI depending on σ_{ele} during summer daytime over typical mountainous regions;
- Figure S16 shows the variations in TAI and LST with elevation standard deviation in typical mountainous regions;
- Figure S17 shows the variations in TAI depending on atmospheric parameters during summer morning;
- Figure S18 gives the variations in TAI depending on typical surface and atmospheric parameters during summer morning;
- Figure S19 shows the differences in LST between Aqua and Terra satellites averaged for multiple days under various weather conditions within a given VZA interval;

- Figure S20 gives the impacts from land cover changes on TAI quantification;
- Figure S21 shows the surface thermal anisotropy curves across mainland China quantified using LST observations from different periods;
- Figure S22 exhibits the impacts from the inherent uncertainties in MODIS LST products on the quantification of TAI;
- Figure S23 shows the impacts from the inherent uncertainties in MODIS LAI and EVI products on examinations of TAI variations with LAI and EVI;
- Figure S24 exhibits the mean TAI curves for 1,708 large inland lakes across different climate zones;
- Figure S25 shows the emissivity directionality of thermal band 31 and 32 in MYD11A1 LST products during summer afternoon;
- Figure S26 shows the Impacts from different classification intervals on the examinations of TAI variations with LAI and SAT;
- Figure S27 shows the TAI variations with SAT during summer afternoons across different climate zones;
- Figure S28 shows the TAI variations with RAD during summer afternoons across different climate zones;
- Figure S29 exhibits the number of LST images within each VZA interval during summertime from 2003 to 2022 across various climate zones.

Text S1: Research progress and challenges of previous studies

Research progress of previous studies

Surface thermal anisotropy has been a subject of scientific inquiry since the 1960s (Monteith & Szeicz, 1962). Research on thermal anisotropy can be broadly grouped into three categories (Cao et al., 2019; Jacob et al., 2008; Paw U, 1992; Wang et al., 2023). (1) Physical modeling: For over half a century, physical models and ground-based or airborne observations have been used to develop effective forward physically process-based methods to investigate thermal anisotropy. These models can be further sub-divided into two categories: those driven by surface component temperatures derived from observations (Kimes et al., 1980; Kimes & Kirchner, 1983; Pinheiro et al., 2004; 2006; Rasmussen et al., 2010; 2011), and those forced by component temperatures simulated through surface energy balance models (Bian et al., 2018; Du et al., 2007; Duffour et al., 2016a; Dyce & Voogt, 2018; Huang et al., 2011; Jiang et al., 2018; Krayenhoff & Voogt, 2016; Lagouarde et al., 2010; 2012; Morrison et al., 2023). These studies typically focused on specific land cover types, particularly vegetation, at relatively small scales. (2) Semi-physical modeling: Within the past decade, semi-physical models, such as kernel-driven models, have successfully combined multiple data sources to simulate or correct thermal anisotropy for predominant land covers, especially vegetation, within satellite overpass regions (Bian et al., 2020; 2021; 2024; Cao et al., 2021; Duffour et al., 2016b; Ermida et al., 2017; 2018; Jiang et al., 2021; Liu et al., 2018; Michel et al., 2023; Vinnikov et al., 2012; Qin et al., 2023; 2025; Wang et al., 2018; 2020). (3) Multi-source data-driven approaches: More recent studies have successfully bypassed a part of physical modeling procedures by leveraging multi-pixel spatial or temporal information to map thermal anisotropy or correct associated directionality (Du et al., 2023; Hu et al., 2016; Teng et al., 2023; Wang et al., 2022; Wang et al., 2023).

Surface thermal anisotropy intensity (TAI) exhibits spatial and temporal variability. For vegetated surfaces, TAI is generally higher in summer than winter, during the day compared to night, and in mid- to low-latitude regions (Na et al., 2024; Wang et al., 2023). The relationship between TAI and vegetation characteristics is complex, with initial increases followed by decreases in TAI as leaf area index and canopy cover increase (Coll et al., 2019; Ermida et al., 2017, 2018; Rasmussen et al., 2010). Topography also plays a significant role, with mountainous areas exhibiting stronger TAI (Ermida et al., 2017; Jiao et al., 2019; Lipton & Ward, 1997; Trigo et al., 2008; Yan et al., 2016). Atmospheric conditions, such as solar irradiance, also influence TAI by affecting temperature gradients between sunlit and shaded areas (Duffour et al., 2016a; Wang et al., 2023).

Challenges of previous studies

Physical models, characterized by high model complexity, usually require detailed surface structure and property information as model input, which has limited their application to larger areas. Semi-physical models have overcome the limitation of elaborate surface property information required by physical models. In addition, recently developed semi-physical models (i.e., dynamic kernel-driven models) have well addressed the interplay of anisotropic thermal radiation and dynamic nature of surface temperature. However, they often rely on either relatively restrictive assumptions about the diurnal temperature cycle patterns or require auxiliary thermal data from geostationary satellites. These restrictions impede their applicability across global lands, especially (1) under complex weather conditions under which the assumptions related to diurnal temperature cycle patterns are invalidated and (2) over high-latitude regions with limited geostationary satellite coverage. Recently proposed multi-source data-intensive models have shown promise in circumventing some of these challenges, but their heavy reliance on the presence of adjacent water bodies or ground-based measurements also restricts their global applicability. As a result, our understanding of thermal anisotropy, a critical land surface property, remains extremely incomplete across different land cover types worldwide.

While significant progress has also been made in interpreting the associations between TAI and related surface and atmospheric parameters, our knowledge of these associations remains predominantly localized. Whether these regional associations can be extrapolated to the global scale remains unverified. Consequently, global-scale statistical associations between TAI and relevant parameters remain unexplored. This knowledge gap significantly hampers accurate angular corrections for satellite-based thermal observations, thereby compromising the applications of thermal remote sensing in various branches of Earth science.

Text S2: Elaborate steps on thermal anisotropy mapping across global lands

Our simple yet effective single-source data-driven methodology comprises a rigorous four-step process (Figure S1 in Supporting Information S1):

Step 1: Removal of outliers in LST observations and binning of VZAs

To reduce the potential uncertainty inherent in LST observations, we identified and removed outliers in time series LST data using the 3σ rule (Na et al., 2024; Xiao et al., 2025). LST observations were divided into 13 viewing VZA bins (10° intervals) from –65° to 65°. LST time series within each VZA bin were then averaged to preliminarily mitigate the impact of rapid atmospheric variations.

Step 2: Further exclusion of LST anomalies and careful selection of valid VZA bins

To further minimize the impacts from LST anomalies and those from varying atmospheric conditions on LST sample counts across VZA bins, additional filtering of VZA bins should be performed. Valid VZA bins were identified through a two-step process. First, daytime LSTs from Aqua generally exceed those from Terra under relatively stable atmospheric conditions. However, LST differences between Aqua and Terra occasionally deviated from the expected patterns. For instance, in some high-latitude regions of the Northern Hemisphere (Figure S19 in Supporting Information S1), Aqua LSTs could be significantly lower than Terra's during the daytime, possibly due to the uncertainties in LST retrievals or atmospheric fluctuations associated with insufficient valid observations. This could introduce potential biases into the TAI quantification. To address this, VZA bins with LST contrasts (Aqua minus Terra) below –1.5 °C or above 10.0 °C were excluded to minimize the impact from LST anomalies (*Criterion #1*; Crosson et al., 2012). The same criteria were applied to nighttime data, but based on LST differences calculated as Terra minus Aqua. Second, a triple weighted standard deviation filter was further applied to identify and further exclude VZA bins with anomalous LST values (*Criterion #2*; Bonamente, 2017; Wang et al., 2006). This filter weighted LST pixels by the number of samples in each VZA bin to calculate weighted mean and standard deviation. We need to clarify that LST data utilized for calculating weighted mean and standard deviation were restricted to a VZA of ±30° for land surfaces beyond 60 °N and 60 °S, mostly due to frequent data anomalies and limited sample sizes at higher latitudes (Wan et al., 2021a; 2021b).

Step 3: Calculation of thermal anisotropy intensity

Thermal anisotropy curves were constructed by mapping LST variations across different VZA bins. Thermal anisotropy intensity (TAI) was quantified as the maximum LST difference between zenith and non-zenith angles (Hu et al., 2016). To enhance TAI accuracy, LSTs across all VZA intervals were smoothed using the LOESS method (Wang et al., 2022) (span = 0.7) in R package. Thermal anisotropy was mapped for all four transit times during both summer (June to August) and winter (December to February) in the Northern Hemisphere, with opposite seasons defined for the Southern Hemisphere.

Step 4: Uncertainty analysis

Our study has employed LST retrievals rather than top-of-atmosphere thermal radiance to map thermal anisotropy. One may question that the derived surface thermal anisotropy can be polluted by the directionality in atmospheric effects. Therefore, we conducted further sensitivity analysis to consolidate that the identified VZA-dependent LST variations are truly from land surfaces rather than due to the directionality in atmospheric effects. Our findings indicate minimal influence from these factors, supporting the robustness of our results. Additionally, we performed sensitivity analyses to examine the potential impacts from retrieval errors in MODIS LSTs, from land cover changes over the study period (2003~2022), as well as from the directionality in emissivity inherent in MxD11 LST products. These analyses demonstrate that such effects are negligible and would not invalidate the main findings of this study.

Text S3: Potential uncertainties related to the impacts from land cover changes over the study period

Our study employed multi-angle LST observations from 2003 to 2022 to map surface thermal anisotropy across global lands. Given the substantial land cover changes (e.g., urban expansion and global greening) observed in many regions worldwide in recent decades, one may question the extent to which such land cover changes could introduce uncertainties into TAI quantification.

To address this, we examined the impacts from land cover change on TAI quantification using mainland China as an example, a region that has undergone particularly pronounced land cover changes in recent decades. Specifically, we examined the TAI patterns during summer afternoon across three periods of varying lengths (2003–2012, 2013–2022, and 2018–2022) and compared them with those derived from the full 2003–2022 period.

The results indicate that the difference in TAI values across different time periods is less than 0.3 °C (Figures S20 and S21 in Supporting Information S1), accounting for only approximately 10% of the overall TAI magnitude observed in this region. While this sensitivity analysis focuses merely on mainland China, we consider that land cover changes during the study period should exert a similarly modest influence on TAI quantification in other regions worldwide. This is because China's urbanization and vegetation greening represent some of the most prominent examples of land cover change worldwide (Chen et al., 2019; Gong et al., 2020).

Text S4: Potential impacts from retrieval errors in various MODIS products

One may question that the inherent uncertainties in MODIS products (e.g., LST, EVI and LAI products) may introduce potential biases into TAI quantification and its relationships with key surface and atmospheric parameters.

To evaluate these uncertainties, we compared the TAI patterns and their variations with LAI and EVI derived from MODIS data with and without quality control, using mainland China as an example. For LST, we utilized only pixels with retrieval errors below 2.0 K according to the QC band of MYD11A1 and MOD11A1. For LAI and EVI, we retained pixels identified as 'good quality' according to the FparLai_QC band of MCD15A3H and the DetailedQA band of MOD13A2.

Our results indicate that the differences in TAI values and their relationships with key parameters are minimal between the quality-controlled and non-quality-controlled datasets. Specifically, the TAI values derived from two methods are 3.27 °C and 3.25 °C, respectively (Figure S22 in Supporting Information S1). Likewise, the TAI variations with LAI and EVI exhibit consistent patterns across both datasets, with only slight numerical differences (Figure S23 in Supporting Information S1). These findings suggest that the potential uncertainties in MODIS products should have a negligible impact on the main conclusions of this study.

Text S5: Potential impacts from directionalities in atmospheric attenuation and emissivity inherent in MODIS LST products

We mapped global land thermal anisotropy using MODIS LST products, rather than relying on top-of-atmosphere raw radiance data. While the LST retrieval algorithm corrects for atmospheric effects using a differential absorption approach in two thermal bands, complete removal of atmospheric influences remains difficult (Hu et al., 2016). Given the dependence of atmospheric attenuation on sensor VZA, one may question that our surface thermal anisotropy estimates may be distorted by directional atmospheric effects.

Inspired by previous insights in eliminating the impacts of directionality in atmospheric attenuation (Hu et al., 2016), we evaluated the uncertainties associated with this effect by mapping thermal anisotropy across 1,708 large inland lakes worldwide using MODIS LST data, because thermal radiation of inland water bodies is mostly isotropic (Hu et al., 2016). Our results reveal an average TAI of 1.3 °C for these lakes during summer daytime (Figure S24 in Supporting Information S1), indeed suggesting a moderate influence of this effect. This value may be jointed induced by the directionality in both emissivity and atmospheric attenuation residual in the MODIS LST products. However, this value is substantially lower than the global mean land surface TAI of around 3.0 °C during the same period (Figures 1a and 1b), indicating that such effects would not largely bias our primary findings.

We also acknowledge that the directional dependence of emissivity in MODIS LST products may also influence the TAI quantification, as emissivity values are determined based on land cover types (Wan et al., 2021a; 2021b) and can vary with viewing geometry. To assess this potential effect, we examined the directional emissivity of bands 31 and 32 in the MYD11A1 product during summer afternoons from 2003 to 2022 across global lands. Our results show that the directionality of emissivity is less than 0.001 for both bands, and occurs only at sensor VZA exceeding ±40° (Figure S25 in Supporting Information S1). According to previous studies (García-Santos et al., 2015; Hu et al., 2019), such minimal variation should exert a negligible impact on TAI quantification.

Text S6: Potential uncertainties related to the interval number for spatially and temporally categorizing MODIS LST pixels

This study examined the TAI variations with LAI and SAT, by spatially or temporally categorizing all LST pixels into different bins according to LAI or SAT values. One may argue that the selection of category number may influence the number of valid pixels within each category, thereby affecting the results.

To address this, we further examined the TAI variations with LAI and SAT by using different number of classification intervals, and compared the results under different interval number. Specifically, for LAI (typically ranging from 0 to 4.5), we adopted three classification schemes, including dividing all LAI into eleven intervals in 0.4 increments, dividing all LAI into nine intervals in 0.5 increments, and dividing all LAI into eight intervals in 0.6 increments. For SAT, we also formulated three classification schemes, including classifying all weather conditions into 6, 8, and 10 categories based on daily SAT values during summer time from 2003 to 2022.

The results indicate that the TAI variations with respect to LAI or SAT across mainland China under different interval number exhibit a broadly consistent pattern across different classification intervals, with only minor numerical differences (Figure S26 in Supporting Information S1). This indicates that while the selection of classification interval may affect the number of valid pixels within each interval, it should exert a relatively minimal impact on the main conclusions of this study.

Text S7: Reasons for the greater TAI variations with SAT than RAD and the relatively low RAD values

One may raise question why TAI variation with SAT appears more pronounced than with RAD, and why the RAD values in Figure 3 are relatively low, which seem contractionary with conventional understanding that RAD strongly regulates surface thermal anisotropy. These patterns, however, may arise from the approach we adopted to examine TAI variations in relation to SAT and RAD. To avoid potential confusion, we provide a more detailed explanation below.

Our analysis reveals that when all grids are included, the magnitudes of TAI variations with SAT and RAD are nearly identical (Figures S27 and S28 in Supporting Information S1). However, in Figure 3, we have narrowed the grid range to more clearly illustrate the TAI variations with weather conditions, which made the SAT-induced variations appear more pronounced.

Specifically, both RAD and SAT are influenced not only by weather conditions but also by geographical locations. In Figure 3, to ensure that the observed TAI variations with SAT and RAD primarily reflect weather-driven changes rather than background climatic differences, we applied additional grid filtering to ensure that the grids were consistent for all SAT/RAD intervals. Since the grid selection for SAT and RAD analyses was performed independently, the grids used for SAT analysis did not overlap with those used for RAD analysis (Figure S3 in Supporting Information S1). Consequently, in the finally chosen grids, the TAI variation with SAT was greater than that for RAD. However, this comparison may not be entirely equitable due to the distinct grids selected for SAT and RAD. This process also led to the exclusion of many grids with high RAD values, resulting in lower RAD values in Figure 3.

Text S8: Clarifications on the robustness of TAI patterns over arid regions

Our results indicate that TAI displays evident spatial variability within arid regions (Figure 2), with desert surfaces typically showing stronger TAI than mountainous or plateau surfaces, which are often characterized by stony or rocky landscapes. One may argue that the relatively lower retrieval accuracy of MxD11 LST products over these hot and dry areas may introduce potential uncertainties into the findings. To address this concern, we provide a detailed explanation from three aspects.

First, our study utilized the MODIS LST V6 product to examine surface TAI across global lands. Compared to the V5 product, the V6 product refined the LST retrieval algorithm for bare soil pixels in hot and warm bare soil zone within latitude between −38° and 49.5° (Wan, 2014). Even if potential retrieval uncertainties may persist in these regions, our analysis focuses on the differential LST between nadir and off-nadir views rather than their absolute values, which could effectively minimize the influence of retrieval errors on TAI quantification.

Second, we performed further sensitivity analyses to demonstrate the relatively minimal impacts from atmospheric attenuation directionality, emissivity directionality, and weather fluctuations on TAI quantification. Specifically, by mapping thermal anisotropy across large inland lakes worldwide, we observed no significant differences in thermal anisotropy patterns between lakes in arid and other climate zones (Figure S24 in Supporting Information S1), indicating the negligible impacts from atmospheric attenuation in arid regions. Additionally, we observed only weak directionality in emissivity for bands 31 and 32 in this region (Figure S25 in Supporting Information S1), suggesting the minimal impact from directional emissivity. Furthermore, there are substantial number of valid observations across all VZAs in arid regions (Figure S29 in Supporting Information S1), signifying the minimal impact from weather fluctuations on TAI quantification.

Third, we further investigated the reasons underlying the notably higher TAI values observed in sandy surfaces compared to mountains and plateaus. This was achieved by examining the individual contributions of several key variables to surface TAI across these typical regions using the widely adopted random forest (RF) model. The selected variables involve three main categories: (1) surface geometries, including surface slope and aspect (i.e., a proxy of azimuth), (2) surface physical properties, including surface albedo and diurnal temperature range of LST (termed DTR_{LST}, a proxy for specific heat capacity), and (3) environmental factors, including downward shortwave radiation and daytime LST (termed LST_{day}). These variables were chosen based on their significant influence on surface TAI and their availability at large spatial scales.

The results showed that surface TAI can be accurately estimated by integrating the RF model with these variables, achieving an R^2 of 0.94 and an RMSE of 0.13 °C. Variable importance analysis revealed that the primary factors regulating TAI across these regions were DTR_{LST} (48%), WSA (26%), and RAD (11%) (Figures S7 and S8 in Supporting Information S1). These findings strongly support our hypothesis that the enhanced TAI over sandy surfaces may be linked to the presence of undulating sand dunes and the lower specific heat capacity of sand. This combination, along with the pronounced solar radiation over arid regions, leads to greater temperature differences between sunlit and shaded components compared to mountainous and plateau terrains.

Importantly, the enhanced TAI observed over sandy surfaces extends beyond the Sahara Desert, with similar patterns found across nearly all sandy regions worldwide (Figure S6 in Supporting Information S1). Notable examples include the Kalahari Desert in southern Africa (Figures S6c and S6d in Supporting Information S1), the Rub' al Khali Desert on the Arabian Peninsula (Figures S6e and S6f in Supporting Information S1), the Karakum Desert in northern Iran (Figures S6e and S6f in Supporting Information S1), the Thar Desert in India (Figures S6e and S6f in Supporting Information S1), and the Taklamakan Desert in China (Figures S6g and S6h in Supporting Information S1). The widespread consistency of these patterns further underscores the robustness of our findings.

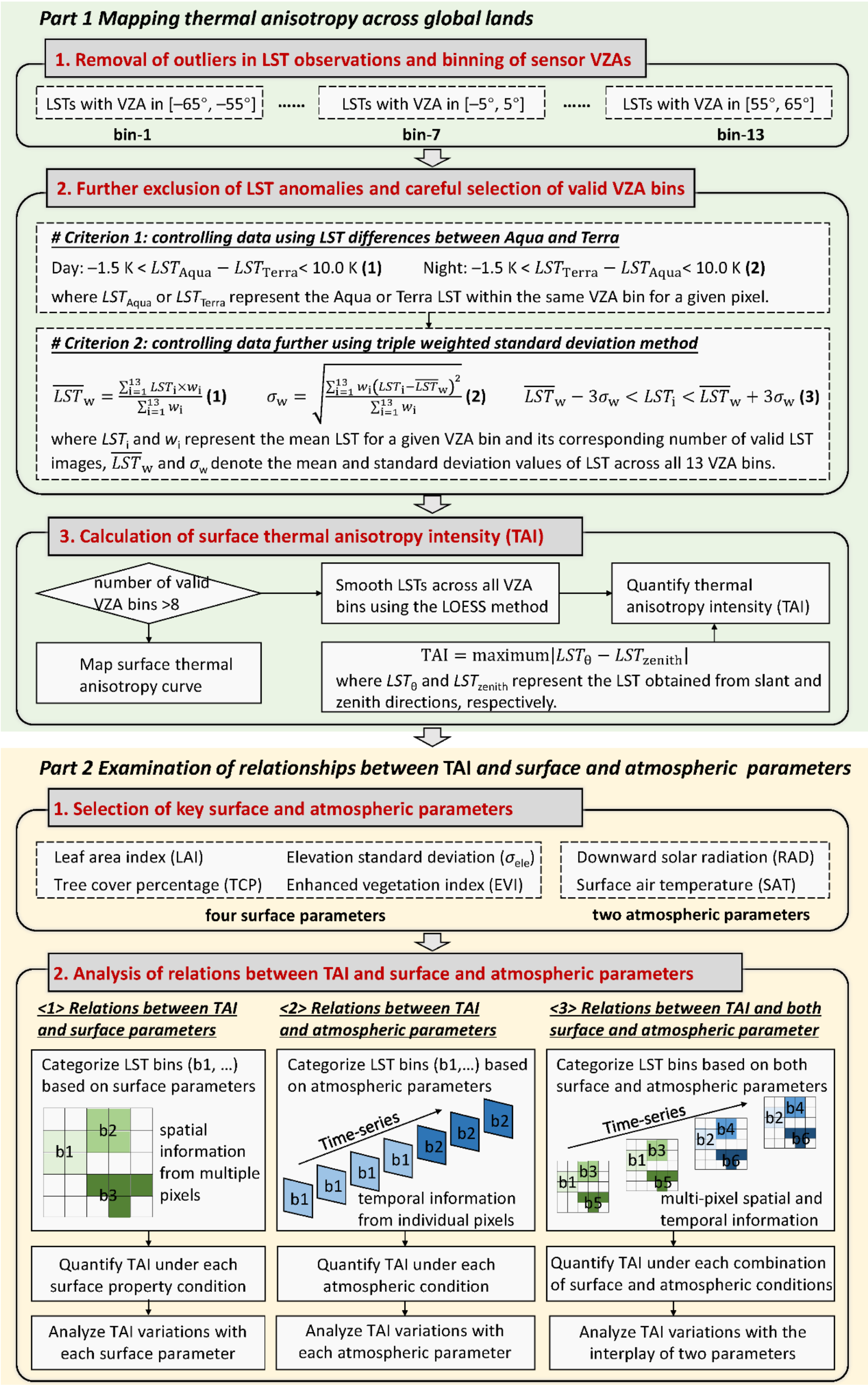

Figure S1. Comprehensive framework for surface thermal anisotropy intensity (TAI) mapping across global lands | The framework comprises two primary components, e.g., mapping of thermal anisotropy (*Part 1*), and analysis of TAI-parameter relationships (*Part 2*). *Part 1* involves three key steps: (1) removal of MODIS land surface temperature (LST) outliers and binning of viewing zenith angles (VZAs), (2) selection of valid VZA bins based on two criteria, and (3) TAI calculation. *Part 2* includes selection of key surface and atmospheric parameters, and identifying relationships between TAI and key surface and atmospheric parameters.

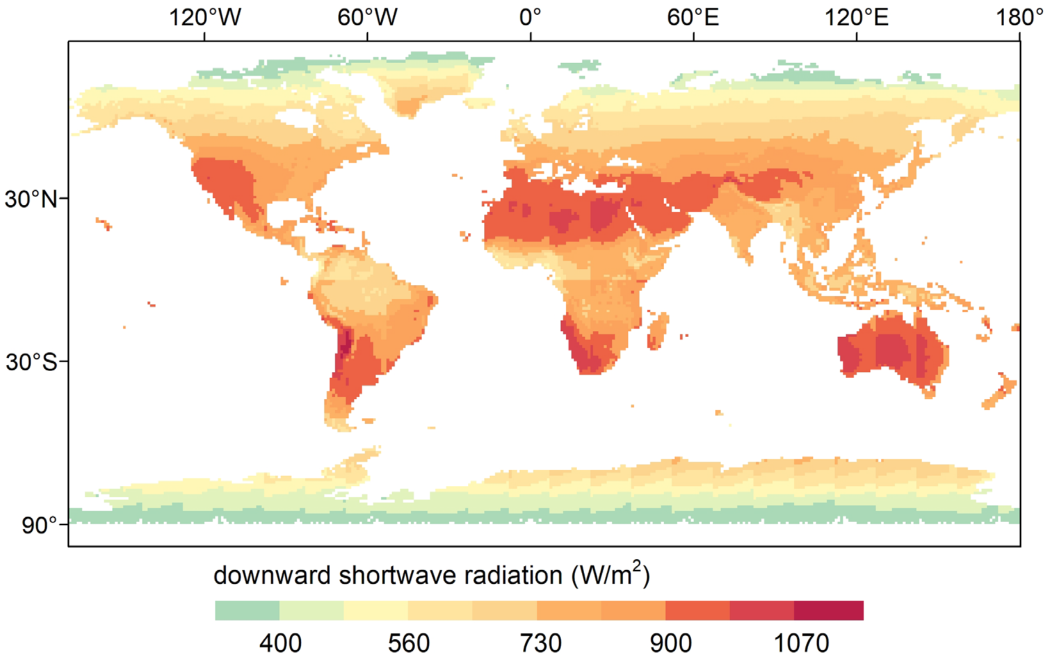

Figure S2. Spatial distribution of downward shortwave radiation (RAD; W/m^2) averaged over all summer afternoons from 2003 to 2022 | These values were extracted from the 2-hour period preceding the Aqua satellite overpass and subsequently masked using daily LSTs from Aqua MODIS to obtain clear-sky values. The observed differences in RAD values across the equator primarily result from the varying definitions of summer months: June to August in the Northern Hemisphere and December to February in the Southern Hemisphere.

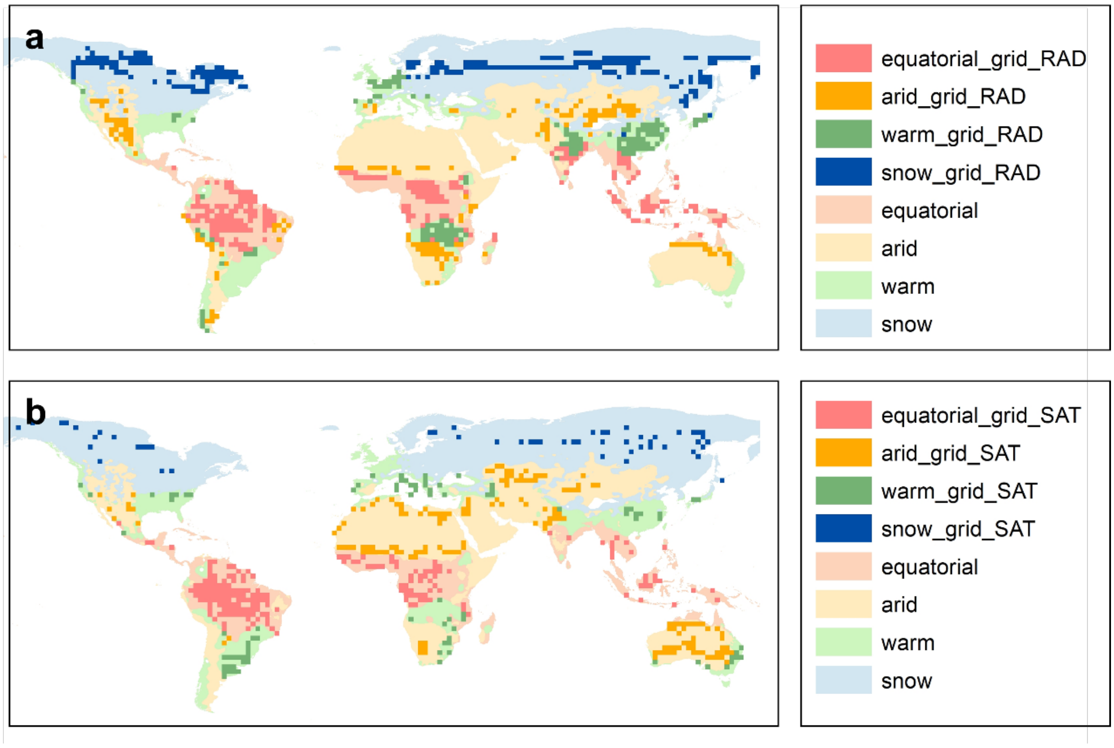

Figure S3. Spatial distribution of the grids used for examining the relationships between TAI and two atmospheric parameters during summer afternoon | The cases for downward shortwave radiation (RAD; a) and for surface air temperature (SAT; b).

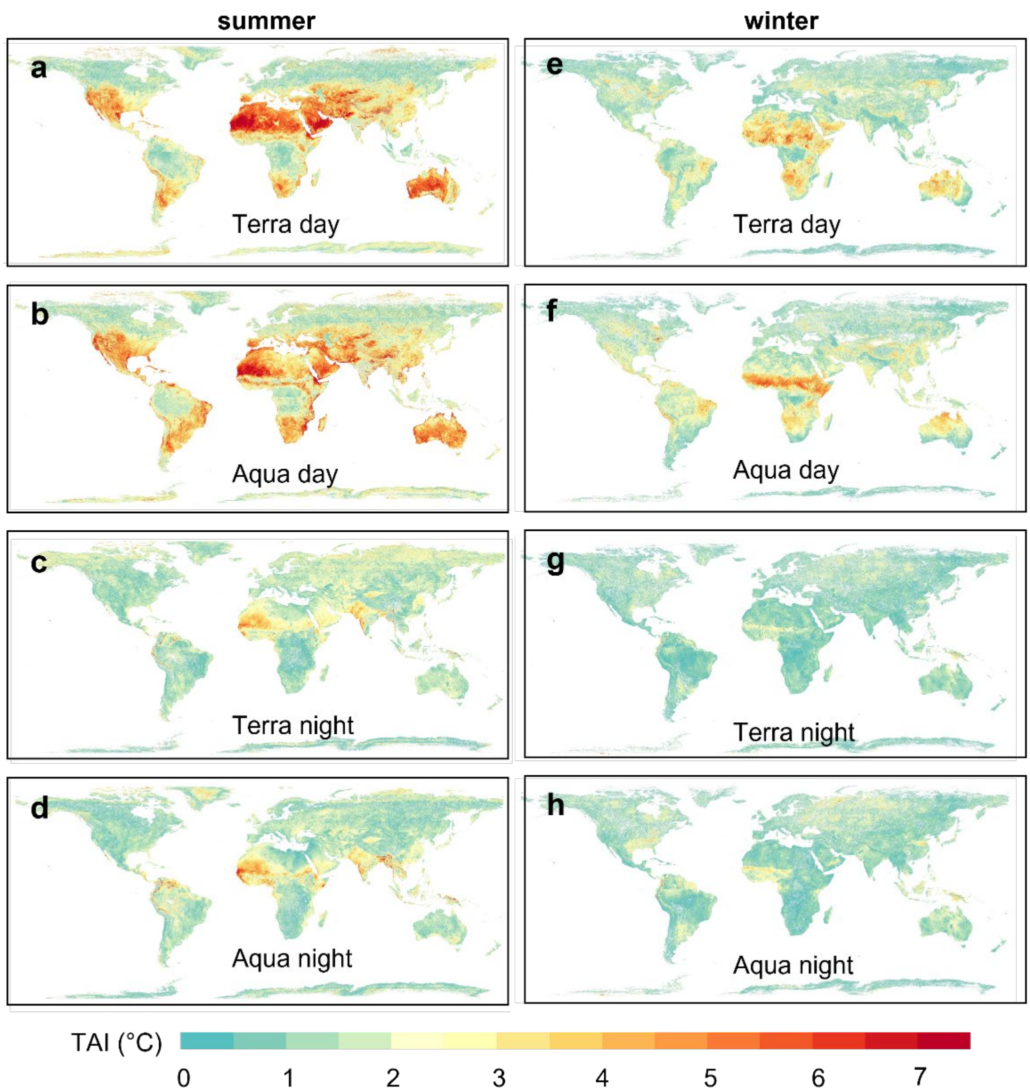

Figure S4. Global mapping of thermal anisotropy intensity (TAI) from 2003 to 2022 | Spatial distribution of TAI for summer (a to d) and winter (e to h), respectively.

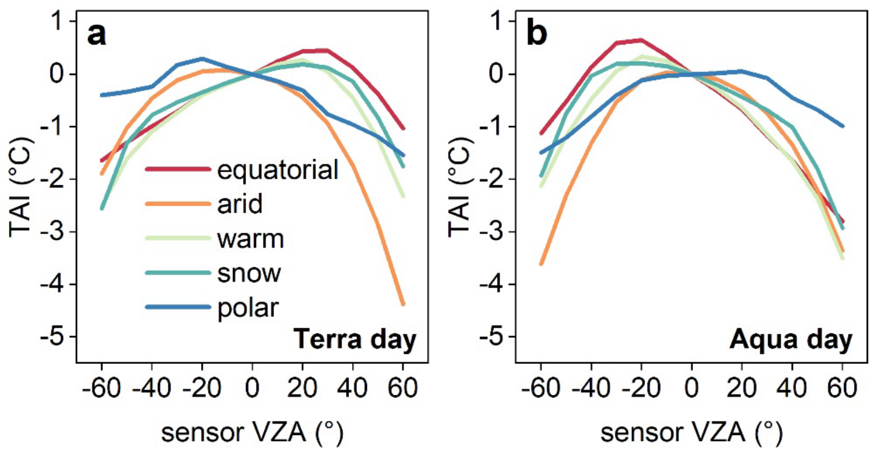

Figure S5. TAI curves for different sensor VZAs during summer daytime across all climate zones | TAI curves for summer morning (Terra; a) and summer afternoon (Aqua; b).

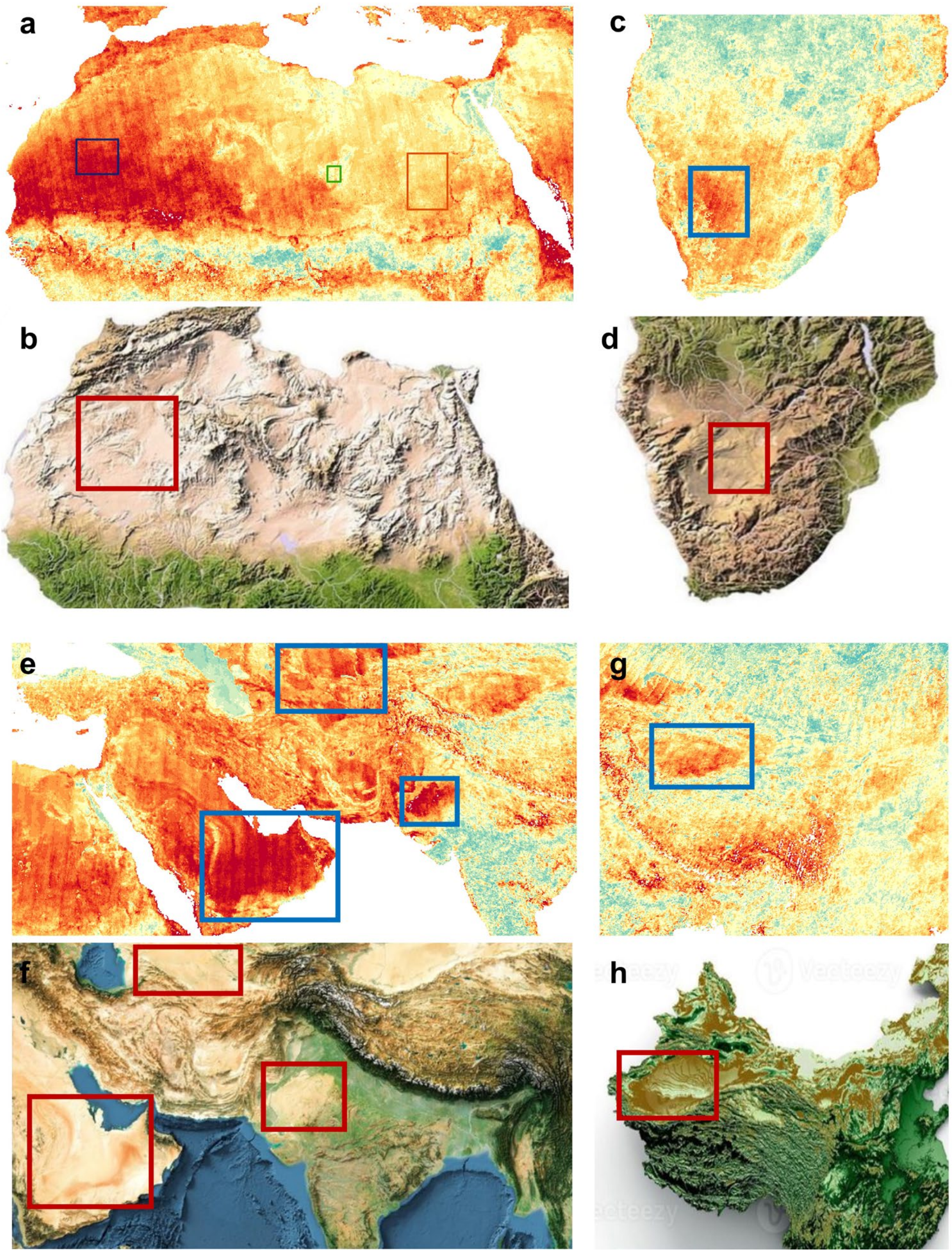

Figure S6. Spatial patterns of TAI during summer mornings over several typical desert surfaces worldwide, alongside their corresponding topographic maps | Cases for the Sahara Desert in Northern Africa (a and b), the Kalahari Desert in Southern Africa (c and d), the Rub' al Khali Desert on the Arabian Peninsula (e and f), the Karakum Desert in Northern Iran (e and f), the Thar Desert in India (e and f), and the Taklamakan Desert in China (g and h). Topographic maps were sourced from https://www.reddit.com/r/MapPorn/comments/blffuv/world_topographic_3d_map/#lightbox.

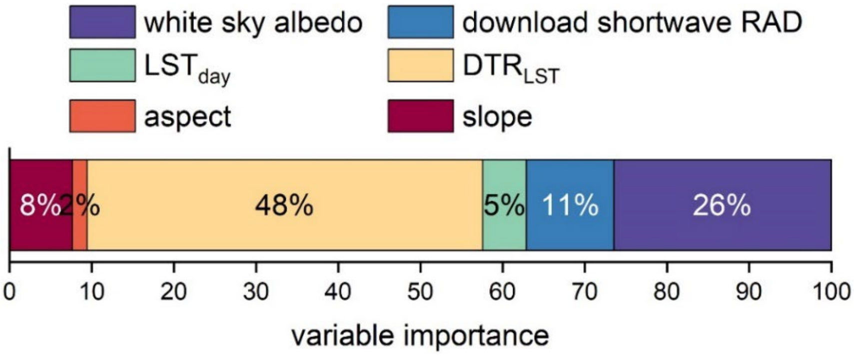

464

465 **Figure S7.** Contributions of various factors to surface TAI across three typical regions
466 of the Sahara Desert (termed Sahara-A, Sahara-B, and Sahara-C).
467

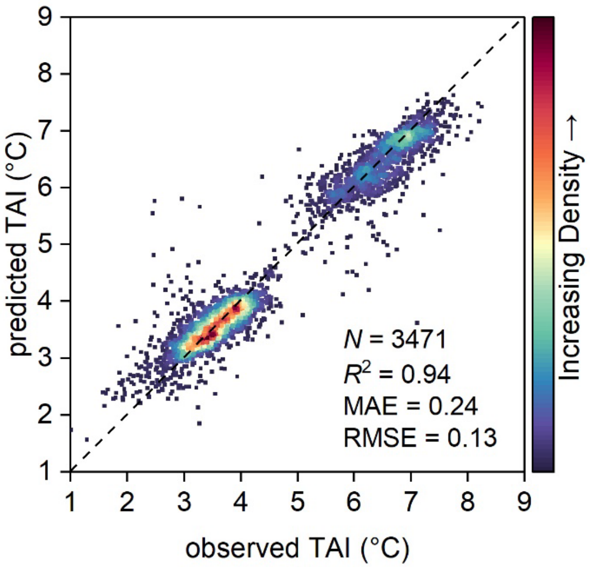

Figure S8. The 1:1 scatterplot comparing the observed and estimated TAI values across three typical regions of the Sahara Desert (i.e., Sahara-A, Sahara-B, and Sahara-C).

Figure S9. Photos of undulating sand dunes over typical deserts | The cases for the Duna en Sossusvlei, Namibia (a; Ragnhild & Neil, 2015) and the Namib desert (b; Diego Delso, 2018).

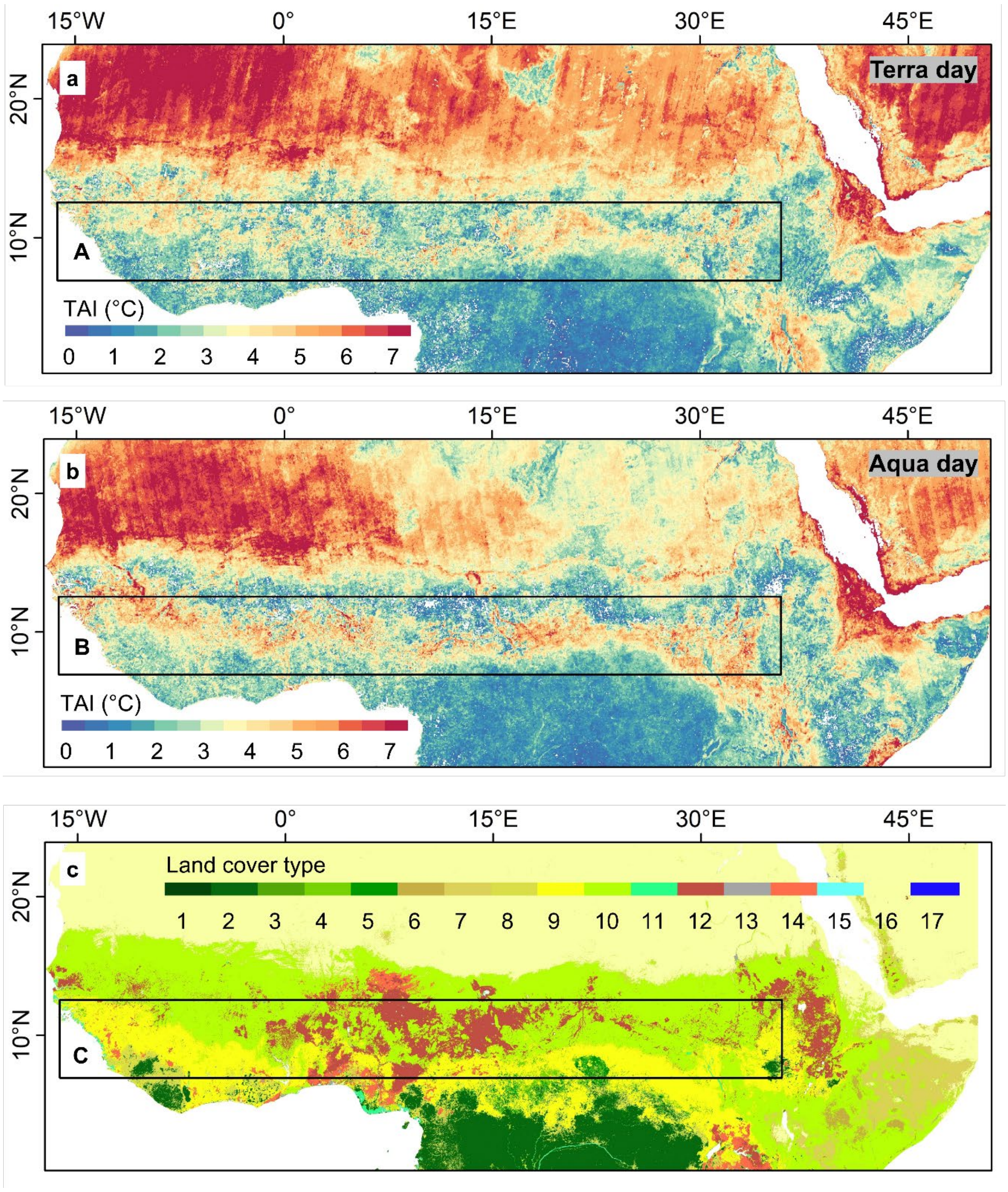

Figure S10. Spatial patterns of TAI during summer mornings (a; Terra) and afternoons (b; Aqua) across typical African regions, alongside the corresponding land cover types (c). The rectangle highlights a west-to-east transect near 10°N, exhibiting a north-to-south sequence of low-high-low TAI patterns. Land cover types are derived from the IGBP classification in the MCD12Q1 product for 2010, with LC_type 9 and 10 representing Savannas (tree cover 10-30%, canopy > 2 m) and Grasslands (dominated by herbaceous annuals, canopy < 2 m), respectively.

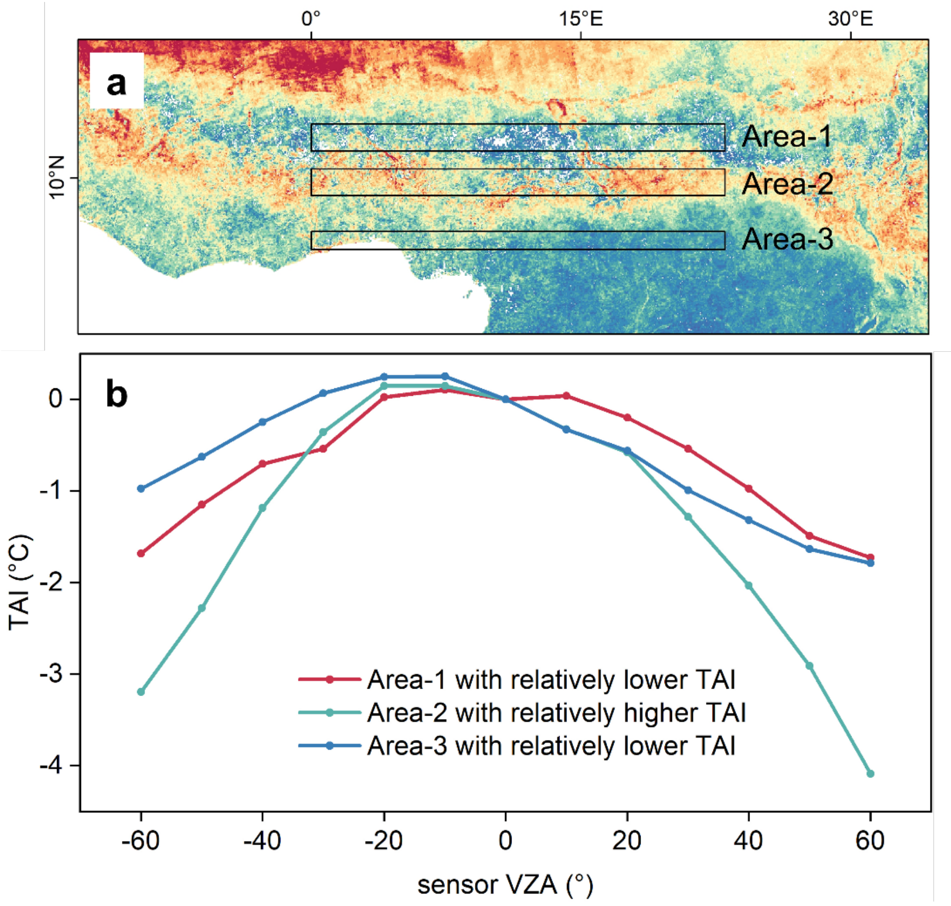

Figure S11. Spatial patterns of TAI (a) across three typical regions: the northern low-TAI region (Area-1), central high-TAI region (Area-2), and southern low-TAI region (Area-3), along with their corresponding thermal anisotropy curves (b) during summer afternoons.

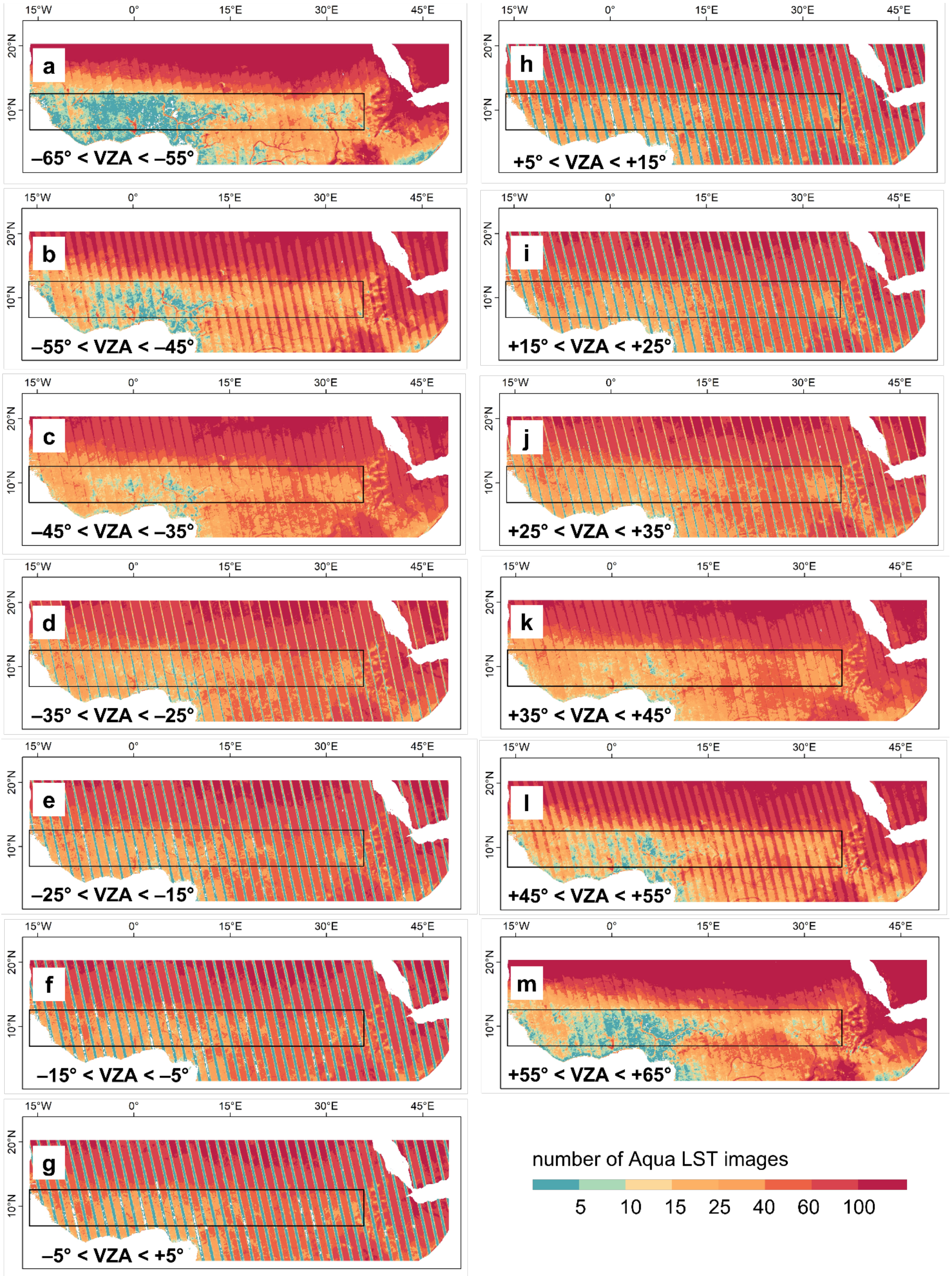

Figure S12. Number of Aqua LST images across different sensor VZA intervals during summertime from 2003 to 2022 over typical African regions. The rectangle highlights a west-to-east transect near 10°N, exhibiting a north-to-south sequence of low-high-low TAI patterns.

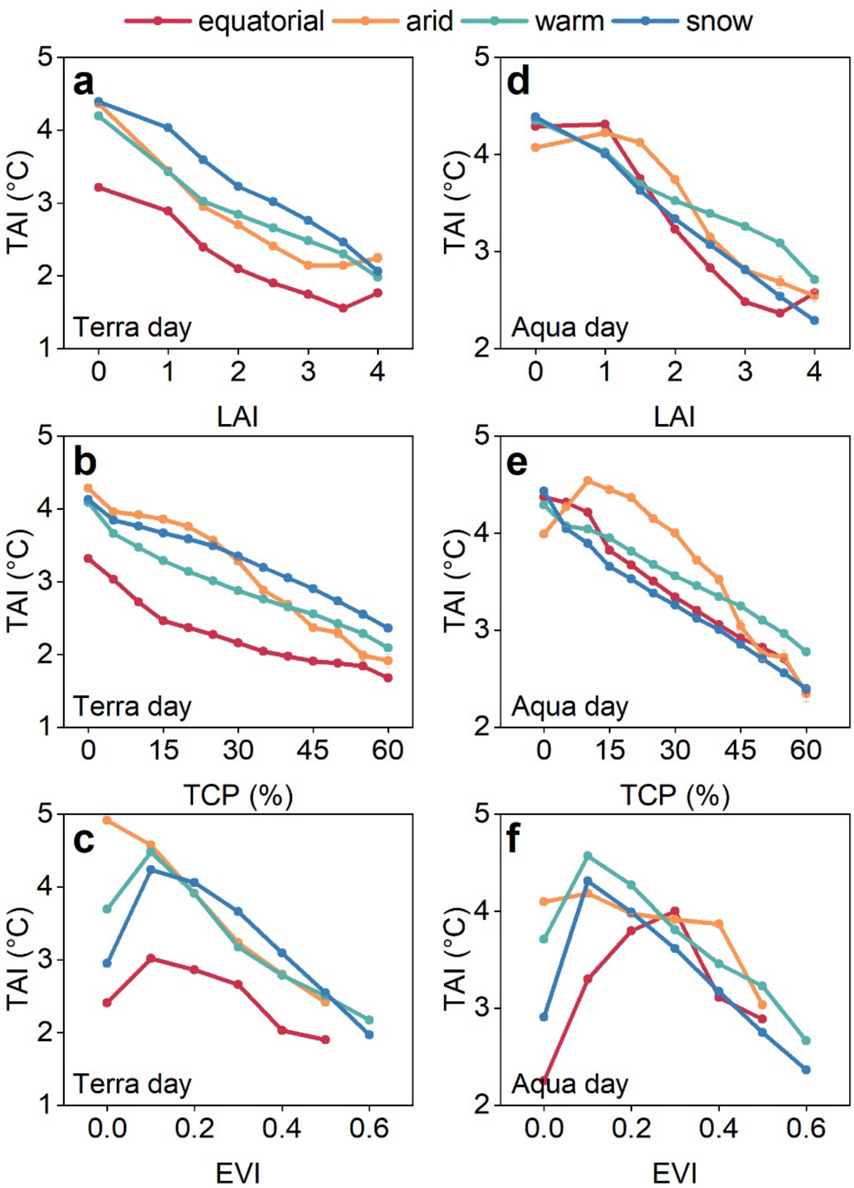

Figure S13. Variations in TAI depending on surface parameters during summer daytime | Variations in TAI with leaf area index (LAI) across different climatic zones during summer morning (a) and afternoon (d); variations in TAI with tree cover percentage (TCP) during summer morning (b) and afternoon (e); and variations in TAI with enhanced vegetation index (EVI) during summer morning (c) and afternoon (f).

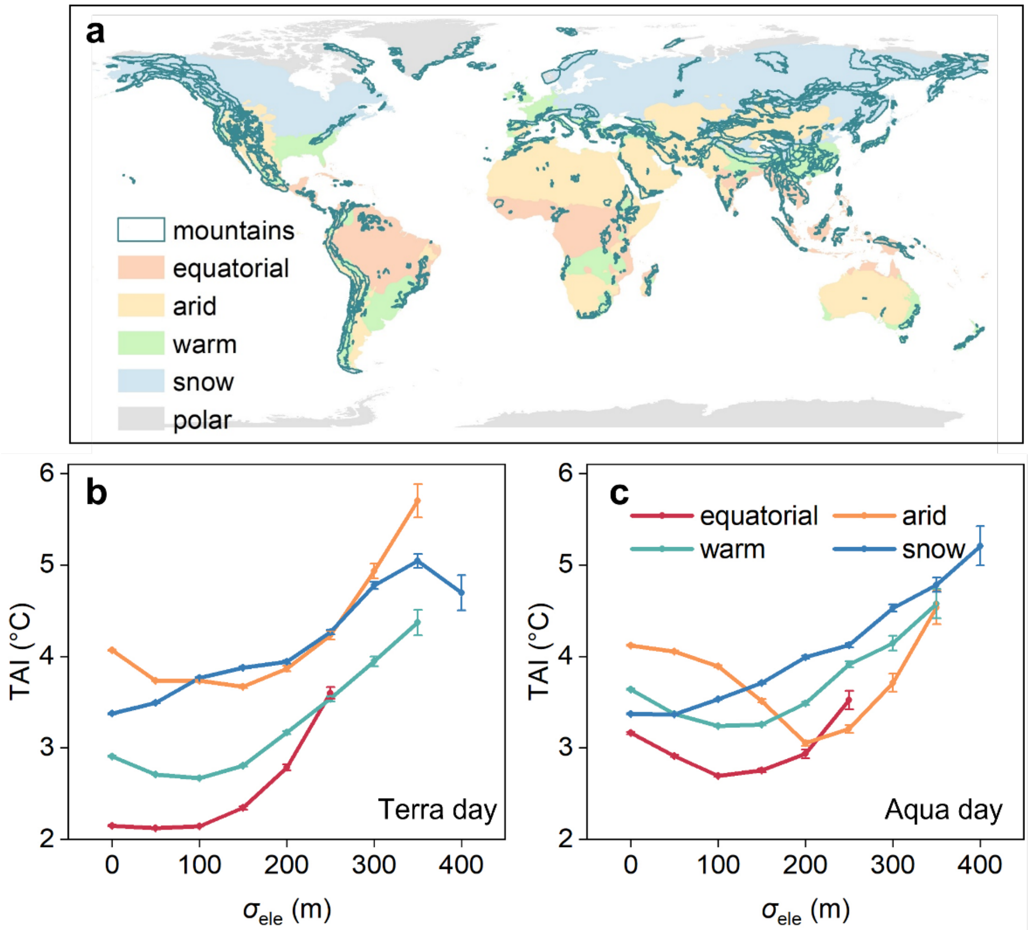

Figure S14. Variations in TAI depending on elevation standard deviation (σ_{ele}) during summer daytime | Distribution of global mountainous surfaces (a) according to the Global Mountain Biodiversity Assessment (GMBA) dataset (Snethlage et al., 2022); and variations in TAI with σ_{ele} across different climatic zones during summer morning (b) and afternoon (c).

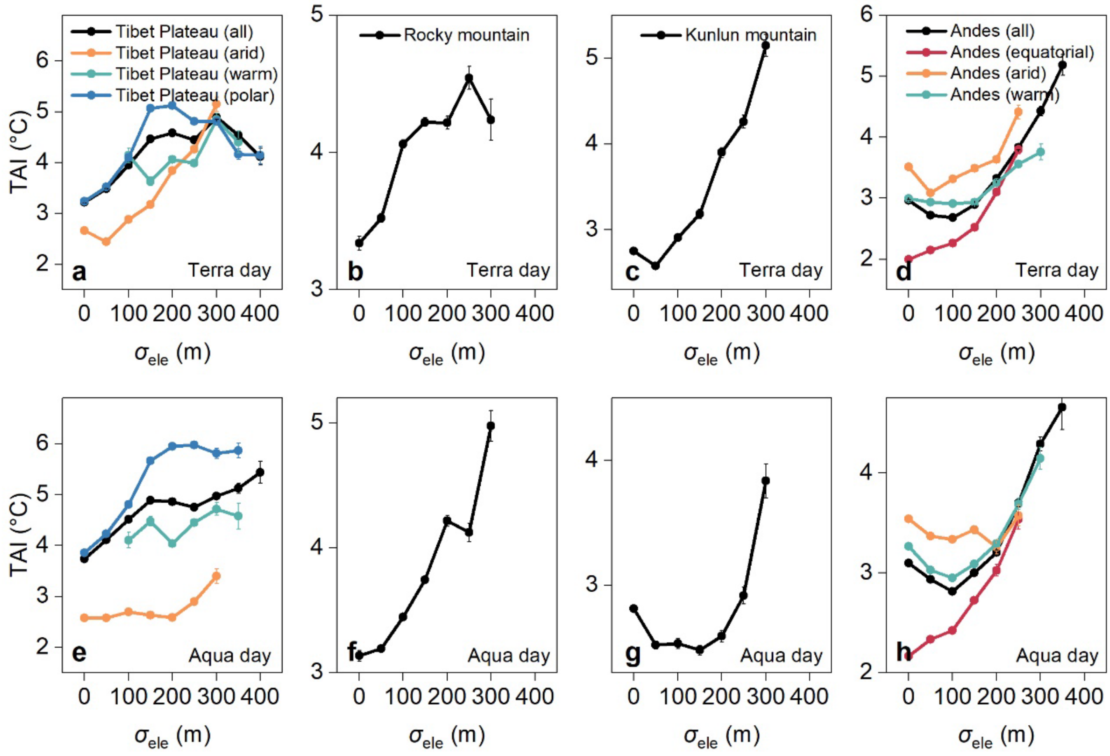

Figure S15. Variations in TAI depending on σ_{ele} during summer daytime over typical mountainous regions | Variations in TAI with σ_{ele} over the Tibet Plateau during summer morning (a) and afternoon (e); variations in TAI with σ_{ele} over the rocky mountains during summer morning (b) and afternoon (f); variations in TAI with σ_{ele} over the Kunlun mountains during summer morning (c) and afternoon (g); and variations in TAI with σ_{ele} over the Andes mountains during summer morning (d) and afternoon (h).

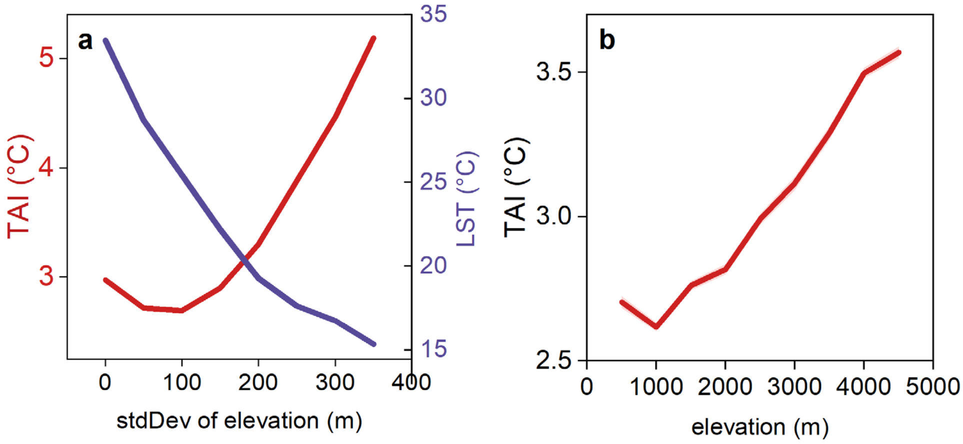

Figure S16. Variations in TAI (red curve) and LST (blue curve) with elevation standard deviation (a), as well as TAI variations with elevation (b) in Andes Mountains.

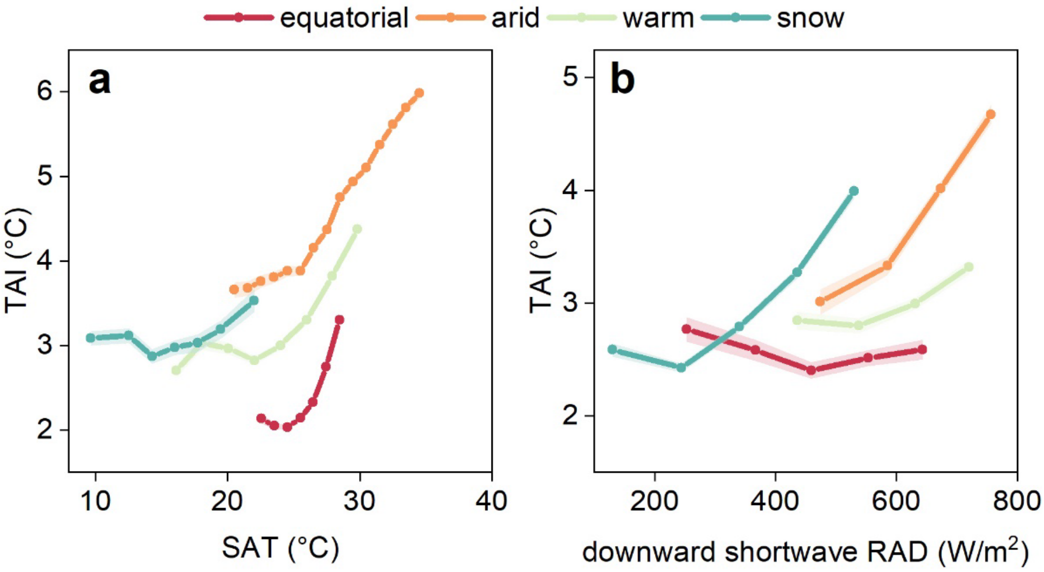

Figure S17. Variations in TAI depending on atmospheric parameters during summer morning | Variations in TAI with surface air temperature (SAT; a) and downward shortwave radiation (RAD; b). Reasons for the relatively low RAD values in (d) are provided in Text S4 in Supporting Information S1.

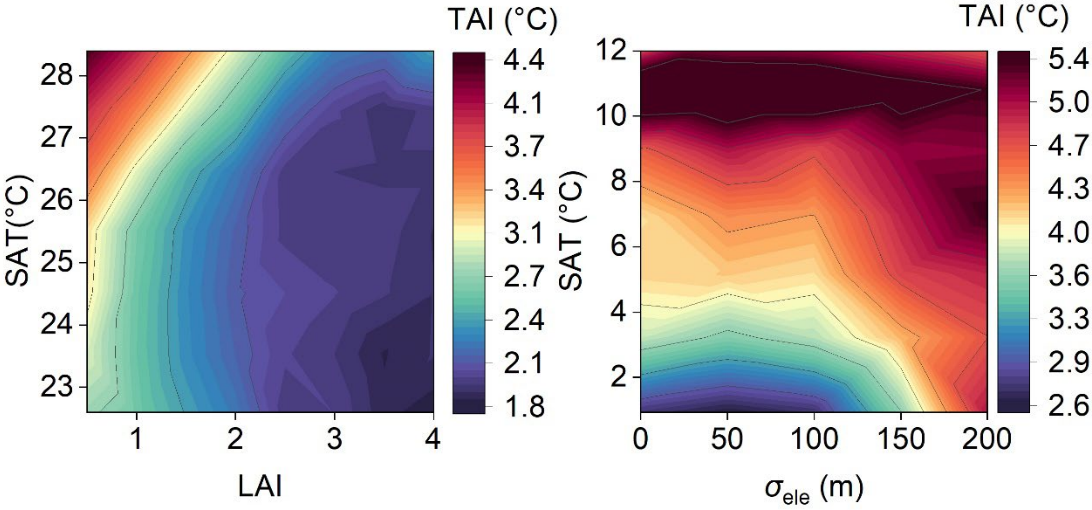

Figure S18. Variations in TAI depending on typical surface and atmospheric parameters during summer morning | Variations in TAI with the interplay between LAI and SAT in tropical climate zones (a); and variations in TAI with the interplay between σ_{ele} and SAT over the Tibetan Plateau (b).

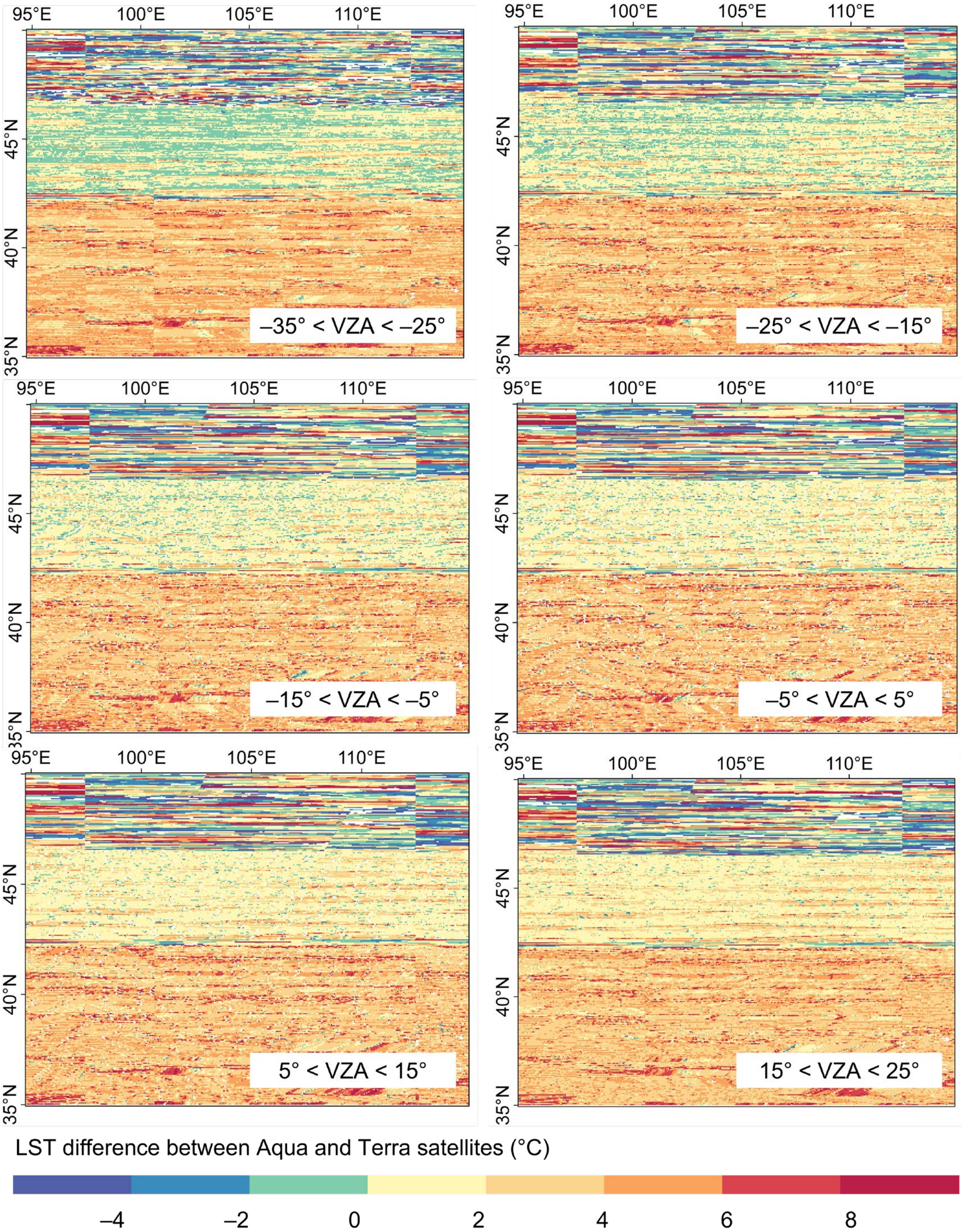

Figure S19. Differences in LST between Aqua and Terra satellites averaged for multiple days under various weather conditions within a given VZA interval, using winter daytime as an example.

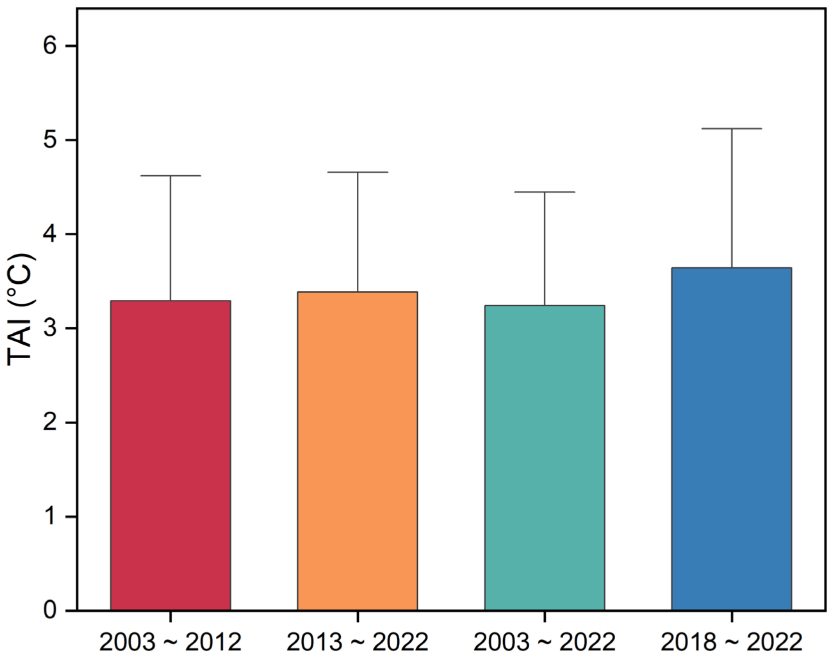

Figure S20. Impacts from land cover changes on TAI quantification | Statistics of surface TAI in mainland China during summer afternoons for the periods of 2003 to 2012, 2013 to 2022, 2003 to 2022, and 2018 to 2022.

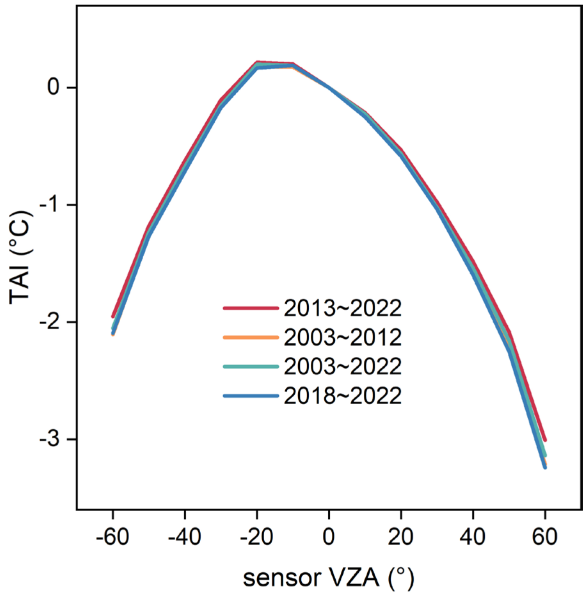

Figure S21. Surface thermal anisotropy curves across mainland China quantified using LST observations from different periods.

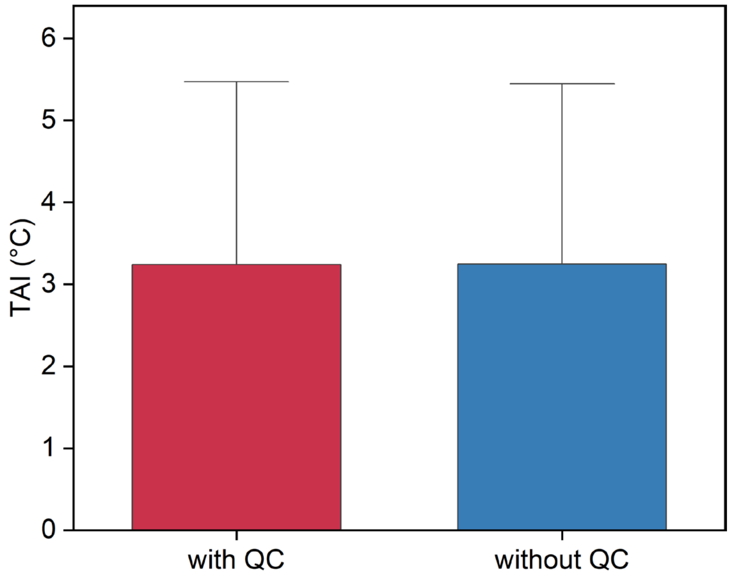

Figure S22. Impacts from the inherent uncertainties in MODIS LST products on the quantification of TAI | Statistics of surface TAI in mainland China derived from raw LST observations (blue column) and quality-controlled LST observations (red column, using pixels with retrieval errors below 2.0 K according to the QC band).

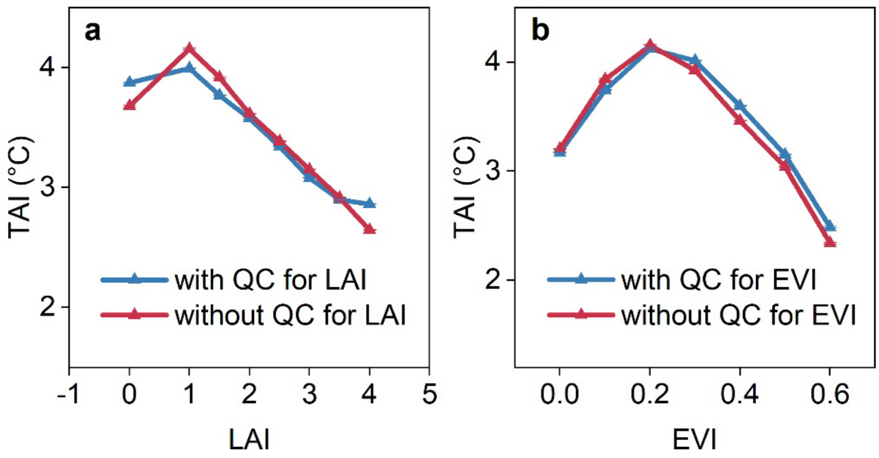

Figure S23. Impacts from the inherent uncertainties in MODIS LAI and EVI products on examinations of TAI variations with LAI and EVI | TAI variations with LAI quantified using LAI data without or with quality control (i.e., pixels labelled as 'good quality' according to the FparLai_QC band) across mainland China (a); TAI variations with EVI quantified using EVI data without or with quality control (i.e., pixels labelled as 'good quality' according to the DetailedQA band) across mainland China (b).

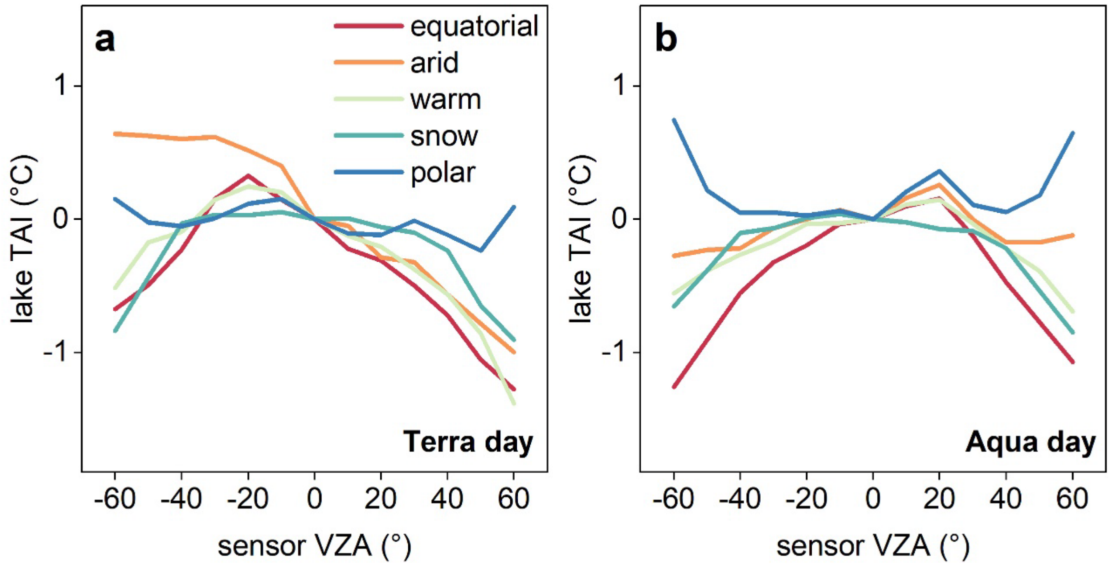

Figure S24. Mean TAI curves for 1,708 large inland lakes across different climate zones during summer morning (a) and afternoon (b).

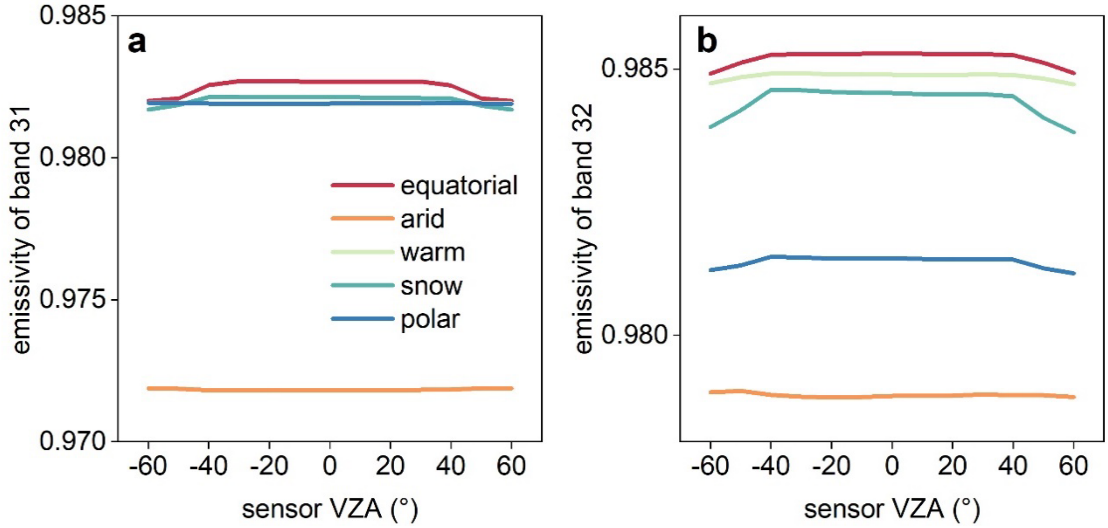

Figure S25. Emissivity directionality of thermal band 31 and 32 in MYD11A1 LST products during summer afternoon | (a) and (b) represent cases for band 31 and 32, respectively.

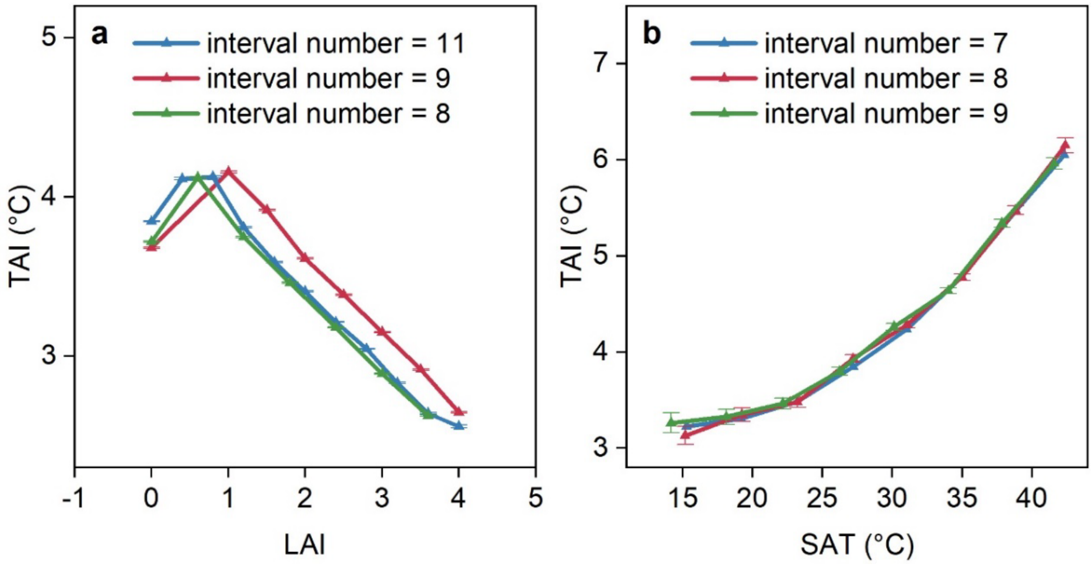

Figure S26. Impacts from different classification intervals on the examinations of TAI variations with LAI (a; using mainland China as a case study) and SAT (b; using arid regions as a case study).

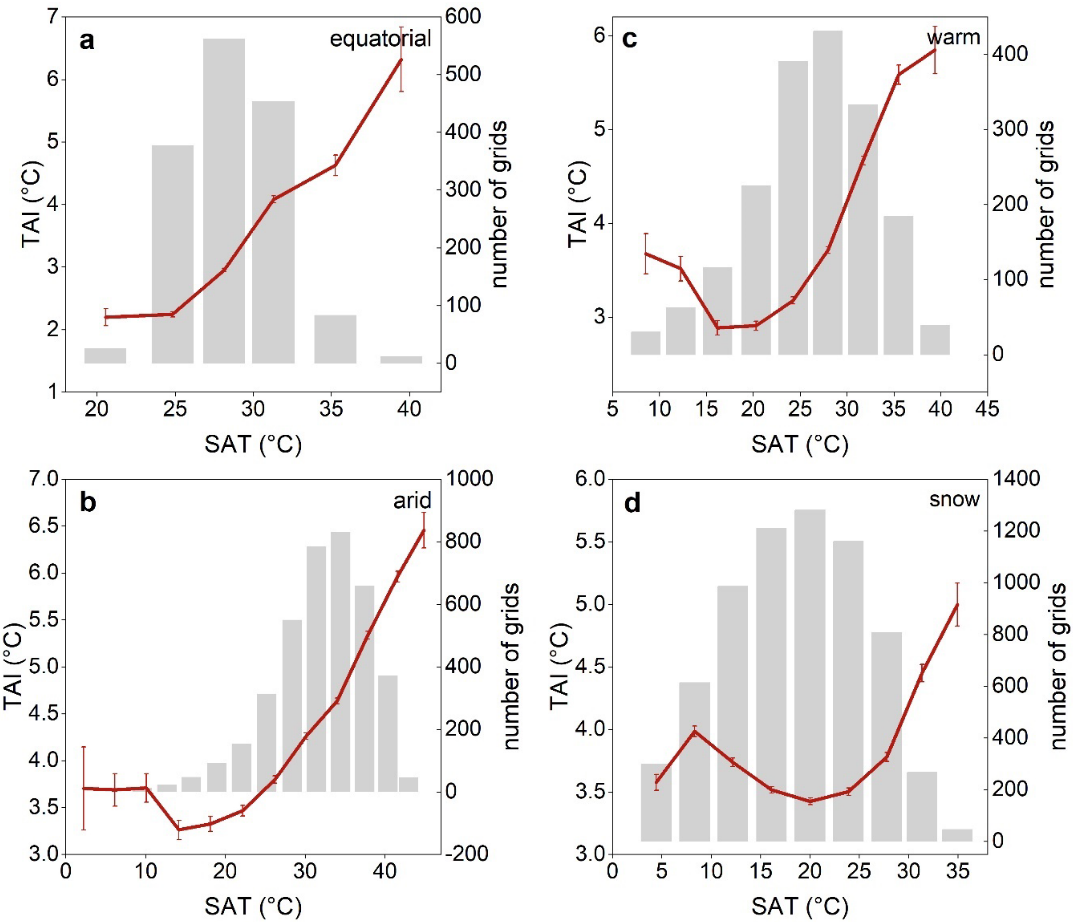

Figure S27. TAI variations with SAT (represented by clear-sky SAT averaged over a 2-hour period prior to Aqua satellite overpasses) during summer afternoons across different climate zones | The red curve depicts the TAI variations in relation to SAT, while the gray histogram represents the number of 2° × 2° grids included in the analysis for each SAT interval.

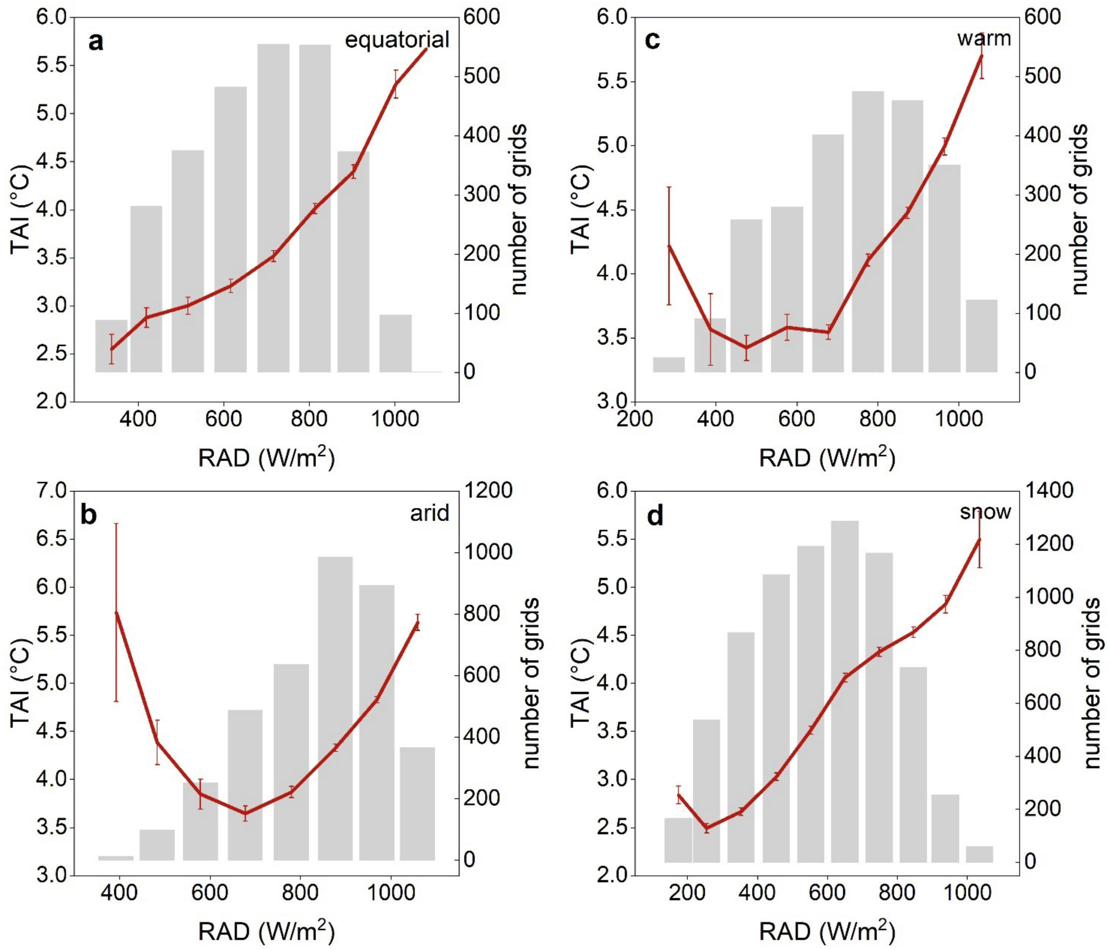

Figure S28. TAI variations with RAD (represented by clear-sky RAD averaged over a 2-hour period prior to Aqua satellite overpasses) during summer afternoons across different climate zones | The red curve depicts the TAI variations in relation to RAD, while the gray histogram represents the number of 2° × 2° grids included in the analysis for each RAD interval.

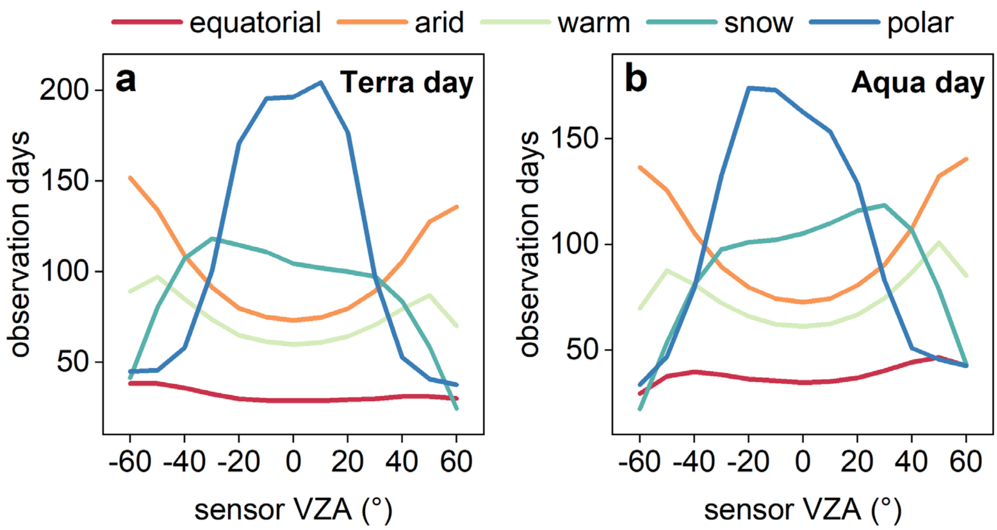

Figure S29. Number of LST images within each VZA interval during summertime from 2003 to 2022 across various climate zones | (a) represents the case for Aqua MODIS, while (b) represents the case for Terra MODIS.